

## Article

# Ti<sub>3</sub>C<sub>2</sub>@g-C<sub>3</sub>N<sub>4</sub>/TiO<sub>2</sub> Ternary Heterogeneous Photocatalyst for Promoted Photocatalytic Degradation Activities

 Yuxin Bai <sup>1</sup>, Shasha Xu <sup>1</sup>, Jing Chen <sup>2,\*</sup>, Xun Sun <sup>3</sup> , Shan Zhao <sup>1</sup>, Jingcai Chang <sup>1,\*</sup> and Zuoli He <sup>1,\*</sup> 

<sup>1</sup> Shandong Key Laboratory of Water Pollution Control and Resource Reuse, Shandong Key Laboratory of Environmental Processes and Health, School of Environmental Science and Engineering, Shandong University, Qingdao 266237, China

<sup>2</sup> The Key Laboratory for Surface Engineering and Remanufacturing in Shaanxi Province, School of Chemical Engineering, Xi'an University, Xi'an 710065, China

<sup>3</sup> Key Laboratory of High Efficiency and Clean Mechanical Manufacture, Ministry of Education, School of Mechanical Engineering, Shandong University, Jinan 250061, China

\* Correspondence: jingchen@xawl.edu.cn (J.C.); changjingcai@sdu.edu.cn (J.C.); zlhe@sdu.edu.cn (Z.H.)

**Abstract:** Ternary heterojunction photocatalysts can improve the transport and separation of photogenerated electrons and holes, which could promote their reduction and oxidation properties for environmental and energy applications. In this research, the ternary photocatalyst Ti<sub>3</sub>C<sub>2</sub>@TiO<sub>2</sub>/g-C<sub>3</sub>N<sub>4</sub> was successfully synthesized via direct electrostatic self-assembly during hydrothermal process. Ti<sub>3</sub>C<sub>2</sub> MXene was used to optimize the interfacial carrier transport and separation between the interfaces. The obtained ternary heterostructured photocatalyst had a higher photocatalytic degradation performance for removing rhodamine B (RhB) and 4-chlorophenol (4-CP). The synergistic effect of heterojunction between g-C<sub>3</sub>N<sub>4</sub> and TiO<sub>2</sub> and Schottky barrier presented among TiO<sub>2</sub> and Ti<sub>3</sub>C<sub>2</sub> suppressed the recombination of the photogenerated electron–hole pairs. Moreover, the Ti<sub>3</sub>C<sub>2</sub> can serve as an active site for the adsorption and activation of organic pollutants resulting from sufficient functional groups (F<sup>−</sup> here).

**Keywords:** Ti<sub>3</sub>C<sub>2</sub>; g-C<sub>3</sub>N<sub>4</sub>; heterojunction; photocatalyst; 4-chlorophenol



**Citation:** Bai, Y.; Xu, S.; Chen, J.; Sun, X.; Zhao, S.; Chang, J.; He, Z. Ti<sub>3</sub>C<sub>2</sub>@g-C<sub>3</sub>N<sub>4</sub>/TiO<sub>2</sub> Ternary Heterogeneous Photocatalyst for Promoted Photocatalytic Degradation Activities. *Coatings* **2023**, *13*, 655. <https://doi.org/10.3390/coatings13030655>

Academic Editor: Alexandru Enesca

Received: 13 January 2023

Revised: 6 March 2023

Accepted: 17 March 2023

Published: 20 March 2023



**Copyright:** © 2023 by the authors. Licensee MDPI, Basel, Switzerland. This article is an open access article distributed under the terms and conditions of the Creative Commons Attribution (CC BY) license (<https://creativecommons.org/licenses/by/4.0/>).

## 1. Introduction

Industrial wastewater seriously affects the environment due to its high concentrations of organic pollutants and substantial toxicity [1–4]. Semiconductor photocatalysis has been widely used to treat industrial wastewater because of its high efficiency, low consumption and environmental friendliness [5–10]. The photocatalysis reaction process involves the excitation, separation, transport and recombination of electron–hole pairs [11,12]. Constructing heterogeneous structures can separate photogenerated carriers, prolonging the lifetime of photogenerated electron–hole pairs with increased reduction and oxidation activities [13–18].

Two-dimensional (2D) materials own unique layered structures and excellent chemical stability, and many researchers have focused on them [19–23]. Among all 2D layered materials, g-C<sub>3</sub>N<sub>4</sub> has demonstrated excellent activity in the photolytic aqua-hydrogen and photocatalytic degradation of organic pollutants due to other excellent optical absorption capabilities and suitable band positions [24–27]. However, the spontaneous recombination of generated electron–hole pairs significantly limits the applications of g-C<sub>3</sub>N<sub>4</sub> in practical photocatalysis [28]. Therefore, the fabrication of heterogeneous photocatalysts with other semiconductors can effectively prevent the recombination of generated electron–hole pairs leading to the promoted overall efficiency [29–31]. Various g-C<sub>3</sub>N<sub>4</sub>-based heterogeneous nanostructures have been synthesized to improve the separation efficiency of photogenerated electron–hole pairs through rapid charge transfer at the interfaces [32–37].

MXene, as a new 2D transition metal carbide or carbon-nitride, was obtained by etching the A-layer in MAX using hydrofluoric acid to obtain the MXene phase [38–41].

Ti<sub>3</sub>C<sub>2</sub>, the most common MXene, possesses a two-dimensional graphene-like structure, leading to its capabilities such as excellent light absorption, electrical conductivity and good hydrophilicity [42–44]. Thus, it has been used as a cocatalyst for photocatalysis reactions. Ti<sub>3</sub>C<sub>2</sub> can also effectively enhance light absorption and promote the separation of photogenerated carriers by forming Schottky junctions [45–47]. MXene-based photocatalysts have been investigated in many different photocatalytic applications, such as the degradation of organic contaminants [48,49], water splitting [50,51], CO<sub>2</sub> reduction [52,53], NO<sub>x</sub> removal [54] and N<sub>2</sub> fixation [55–57].

Our previous research showed TiB<sub>2</sub>-TiO<sub>2</sub>@g-C<sub>3</sub>N<sub>4</sub> (TBCN) ternary heterojunction composites with promoted photocatalytic degradation performances for RhB and 4-CP removal [58]. Herein, new Ti<sub>3</sub>C<sub>2</sub>@TiO<sub>2</sub>/g-C<sub>3</sub>N<sub>4</sub> (TC-TBCN) ternary heterostructured photocatalysts were synthesized through the direct electrostatic self-assembly of TBCN with Ti<sub>3</sub>C<sub>2</sub> via a hydrothermal process; the addition of Ti<sub>3</sub>C<sub>2</sub> could effectively enhance light absorption and promote the transfer of photogenerated carriers by forming Schottky junctions with TBCN. The morphology, pore structure, phase composition, optical properties and photocatalytic performances of the TC-TBCN photocatalysts were investigated. The obtained ternary Ti<sub>3</sub>C<sub>2</sub>@TiO<sub>2</sub>/g-C<sub>3</sub>N<sub>4</sub> photocatalysts could effectively improve the separation and migration efficiency of photogenerated charges, and its large surface active sites and effective interfacial charge transfer showed a better photodegradation performance for both rhodamine B (RhB) and 4-chlorophenol (4-CP), providing an essential idea for degrading pollutants and treating organic wastewater. Finally, we propose the mechanism of the photocatalytic degradation of such ternary photocatalysts.

## 2. Materials and Methods

### 2.1. Chemicals

Titanium aluminum carbide (Ti<sub>3</sub>AlC<sub>2</sub>) powders were purchased from Laizhou Kai Ceramic Materials Co., Ltd. (Yantai, China). Hydrofluoric acid (HF, 40%), titanium boride (TiB<sub>2</sub>), melamine (C<sub>6</sub>H<sub>6</sub>N<sub>6</sub>, ≥ 99.0%), anhydrous ethanol (C<sub>2</sub>H<sub>5</sub>OH), rhodamine B (RhB), 4-chlorophenol (4-CP), silver nitrate (AgNO<sub>3</sub>), isopropyl alcohol (IPA), benzoquinone (BQ) and disodium ethylenediaminetetraacetate (EDTA-2Na) were all purchased from Aladdin Chemical Reagent Co., Ltd. (Shanghai, China). All chemical reagents were of analytical grade (AG) and used without other treatments in our experiments.

### 2.2. Synthesis of Catalysts

#### 2.2.1. Synthesis of TBCN

Our previous research reported on TiB<sub>2</sub>-TiO<sub>2</sub>@g-C<sub>3</sub>N<sub>4</sub> (TBCN) composites with core-shell structures, the synthesis process of which is presented in Figure 1 [58]. The mass ratio of TiB<sub>2</sub> to melamine was 1:100 in this experiment. Firstly, 0.1 g TiB<sub>2</sub> and 10 g melamine powders were ground for 10 min to form a uniform mixed powder. Then, the obtained gray powder was transferred to a crucible with a cover and wrapped using aluminum foil, and then it was calcinated at 550 °C for 5 h in a muffle furnace in air. g-C<sub>3</sub>N<sub>4</sub> was grown in situ on the TiB<sub>2</sub> surface, making a g-C<sub>3</sub>N<sub>4</sub> coating on the TiB<sub>2</sub> core, and the products were obtained after washing and drying, here named TBCN.

#### 2.2.2. Synthesis of Ti<sub>3</sub>C<sub>2</sub>

As shown in Figure 1, 1.0 g of Ti<sub>3</sub>AlC<sub>2</sub> powder (MAX phase) was put in a PTFE reactor; then, 20 mL of a 40% HF solution was added for etching the Al layer. The solution was stirred for 3 days at room temperature. Then, the pH of the obtained suspension could be tuned to pH ≥ 6 using lots of deionized (DI) water. Finally, the resulting black Ti<sub>3</sub>C<sub>2</sub>F<sub>x</sub> powder was dried in an oven after washing with ethanol through centrifugation for use in the next step.

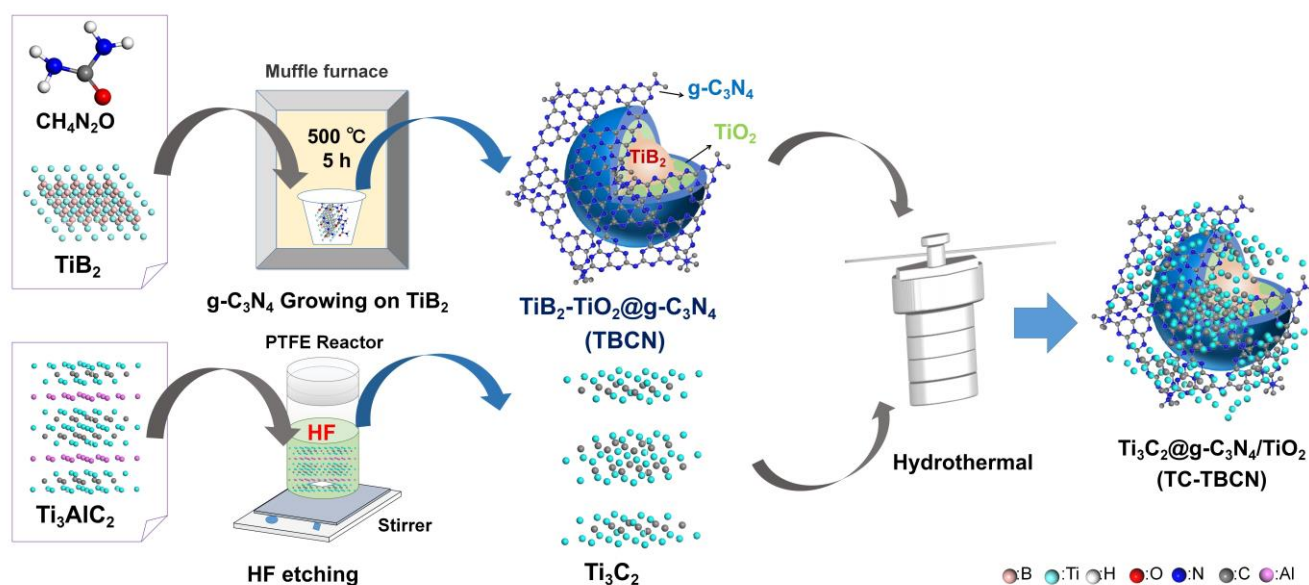


**Figure 1.** Schematic of the synthesis process for TC-TBCN composite.

### 2.2.3. Synthesis of TC-TBCN

The TC-TBCN was synthesized via a hydrothermal process, as shown in Figure 1, where 0.2 g of TBCN powder and a given amount of  $\text{Ti}_3\text{C}_2\text{F}_x$  powder were added into 60 mL of DI water under stirring, followed by ultrasonication to obtain the dispersed suspension. Then, the suspension was transferred to a Teflon-lined stainless-steel autoclave and maintained at 120 °C for 12 h. A solid yellow powder deposited at the bottom was collected and washed thoroughly with deionized water after the autoclave cooled down. The final TC-TBCN products were obtained after drying in a vacuum drying oven. The mass ratios of  $\text{Ti}_3\text{C}_2\text{F}_x$  and TBCN were 0 wt%, 1 wt%, 2.5 wt%, 5 wt% and 10wt%, and were designated as 1-TBCN, 1TC-TBCN, 2.5TC-TBCN, 5TC-TBCN and 10TC-TBCN, respectively.

### 2.3. Characterization

The morphologies of the obtained products were conducted on scanning electron microscopy (SEM, FEI Quanta FEG 250, Hillsboro, OR, USA) and transmission electron microscopy (TEM, JEOL JEM-2100, Tokyo, Japan). An X-ray diffraction spectrometer (XRD, Bruker D8 ADVANCE, Karlsruhe, Germany) was used to determine the crystal phases. The synthesized photocatalysts' surface composition and elemental chemistry were measured on an X-ray photoelectron spectrometer (XPS, Thermo Scientific K-Alpha+, Waltham, MA, USA) equipped with a monochromatic Al K  $\alpha$  X-ray source (1486.6 eV). The XPS spectra were calibrated with the C1s peak of amorphous carbon (284.6 eV) and fitted using XPSPEAK 4.1 software. The UV-Vis absorption spectra were obtained with a UV-Vis spectrophotometer (UV-Vis, Shimadzu UV2600, Kyoto, Japan). A specific surface area analyzer (JW-BK200B, Beijing JWGB Sci&Tech Co., Ltd., Beijing, China) was used to determine the Nitrogen adsorption-desorption isotherms, and the specific surface area and pore size distribution were obtained based on the Brunauer-Emmett-Teller (BET) method and Barret-Joyner-Halenda (BJH) method. Fourier transform infrared spectra (FTIR) were obtained using a FTIR spectrophotometer (Thermo Scientific Nicolet iS50, Waltham, MA, USA), equipped with an ATR accessory.

### 2.4. Photocatalytic Performance Measurements

RhB and 4-CP were used as target pollutants to evaluate the photocatalytic ability of the obtained photocatalysts in a Pyrex reactor with a volume of 57.5 mL. The detailed experiment was as follows: In total, 20 mg of the photocatalyst was dispersed in 36 mL DI water under sonication for 2 min; then, 4 mL of 100 ppm RhB or 4-CP solution was added and stirred in the dark for 30 min to establish an adsorption-desorption equilibrium

of the pollutants. The light source for the photoreaction was a 300 W Xe lamp equipped with a VisREF filter (350 nm–780 nm). The reacted solution was magnetically stirred during the photocatalytic reaction. In total, 1.0 mL sample suspensions were taken from the reactor intermittently in specific time intervals and filtered through a 0.22  $\mu\text{m}$  pore-sized PTFE syringe filter to determine the removal rate of the pollutants. A UV–Vis spectrophotometer (Shimadzu UV2600, Kyoto, Japan) was used to determine the absorbance of the resulting RhB solution at the characteristic wavelength (554 nm). The changes in absorbance values quantitatively were used to calculate the degradation percentage. In contrast, the 4-CP concentration was determined on a high-performance liquid chromatography system (HPLC, LC-2030Plus, Shimadzu, Kyoto, Japan) equipped with a Shim Pack C18 column using a UV–Vis detector (measurement details: column temperature: 35  $^{\circ}\text{C}$ ; mobile phase: acetonitrile-0.1 vol. % acetic acid 60:40 (*v:v*); flow rate: 1.0 mL/min; detect wavelength: 280 nm). Incidentally, the  $\text{Cl}^-$  was also determined using the ion chromatograph (IC, Shine CIC-D120, Qingdao, China) equipped with a Shine SH-AC-3 column with conductivity detection (measurement details: mobile phase: column temperature: 35  $^{\circ}\text{C}$ ; 2.4 mM  $\text{Na}_2\text{CO}_3$  + 1.0 mM  $\text{NaHCO}_3$  aqueous solution; flow rate: 1.0 mL/min; current: 30 mA). Finally, photocatalytic efficiency was calculated according to the concentration changing ( $C/C_0$ ), where  $C$  and  $C_0$  are the measured and initial concentrations of RhB and 4-CP, respectively. The final degradation efficiency of RhB could be calculated according to the Lambert-Beer law.

### 3. Results

#### 3.1. Structure Characterization

##### 3.1.1. Structure and Composition of $\text{Ti}_3\text{C}_2$

Scanning electron microscopy (SEM) was used to investigate the morphologies of the MAX and MXene phases. As shown in Figure 2, the  $\text{Ti}_3\text{AlC}_2$  powders were measured with any other treatments. As shown in Figure 2a, the original  $\text{Ti}_3\text{AlC}_2$  MAX possessed an irregular blocky layered structure. After HF etching, the  $\text{Ti}_3\text{C}_2$  MXene exhibited a nanosheet-like layer structure, with some thin nanosheets clearly shown in Figure 2b, which was significantly different from the MAX phase, indicating that the HF etching could remove the Al atom layer sandwiched in between the MAX layers [59].

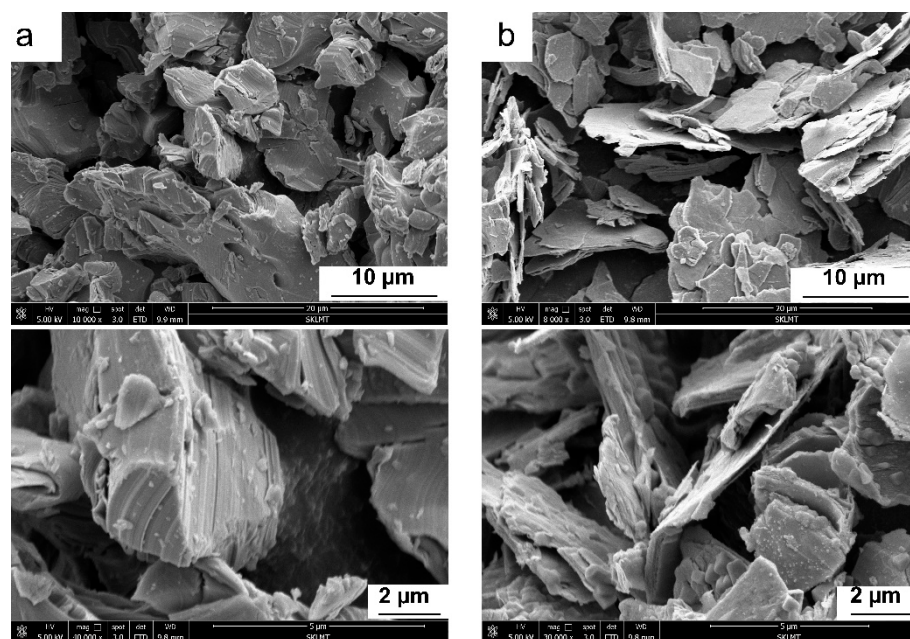


**Figure 2.** SEM images of  $\text{Ti}_3\text{AlC}_2$  before (a) and after (b) HF etching for 72 h.

Figure 3a shows the XRD patterns of the  $\text{Ti}_3\text{AlC}_2$  before and after being etched in the HF solution. The diffraction peaks of the  $\text{Ti}_3\text{AlC}_2$  located at  $9.5^{\circ}$ ,  $19.2^{\circ}$ ,  $35.9^{\circ}$ ,  $38.8^{\circ}$  and  $41.7^{\circ}$

belonged to the different crystal planes (002), (004), (101), (104) and (105), respectively. The characteristic peaks of  $\text{Ti}_3\text{AlC}_2$  located at  $9.5^\circ$  and  $19.2^\circ$  shifted to lower angles, and the intensity was decreased after HF etching [60]. The highest diffraction peak at  $38.8^\circ$  from the (104) crystal plane disappeared, indicating the successful preparation of  $\text{Ti}_3\text{C}_2$  via a complete Al layer etching [61]. In addition, the red curve was the XRD pattern of the  $\text{Ti}_3\text{C}_2\text{F}_x$  MXene sample. The peaks matched well with those of  $\text{Ti}_3\text{C}_2\text{F}_x$  synthesized by others [62].

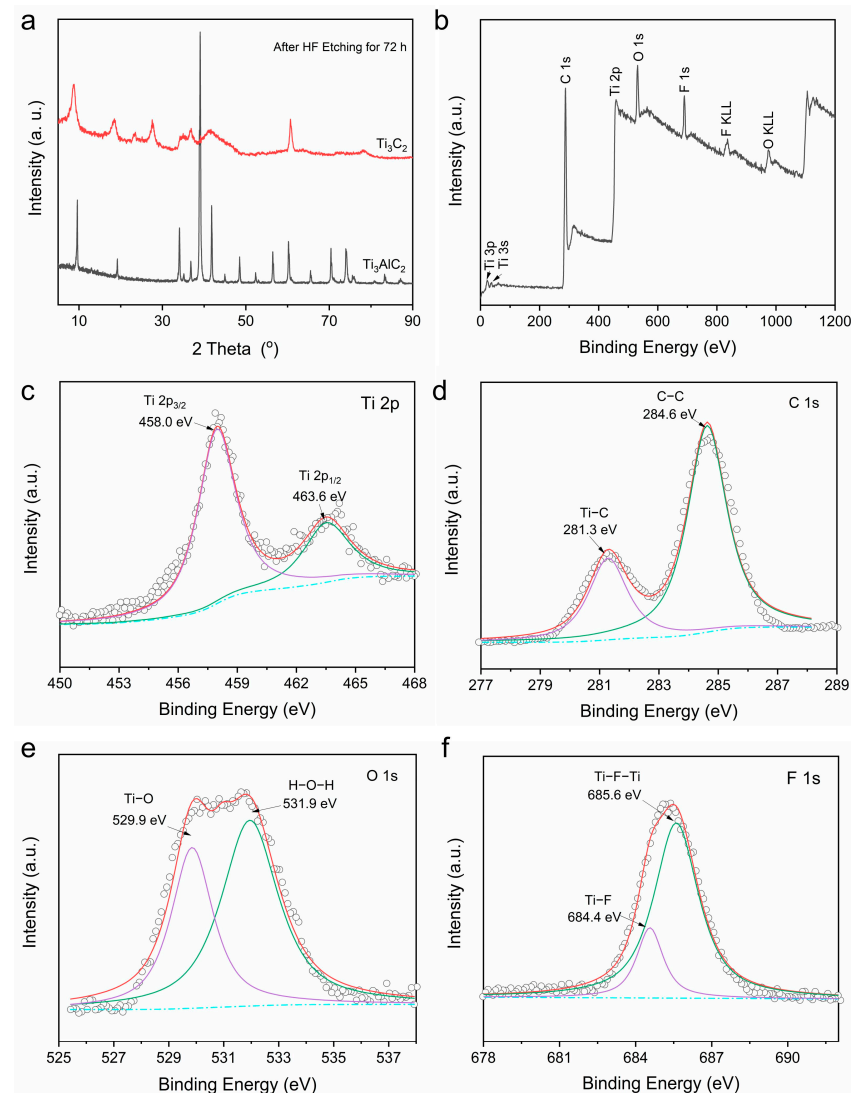


**Figure 3.** (a) XRD patterns of the MAX phased  $\text{Ti}_3\text{AlC}_2$  before and after being etched in HF solution; XPS spectra of  $\text{Ti}_3\text{C}_2$ : (b) survey; (c) Ti 2p; (d) C 1s; (e) O 1s; (f) F 1s.

An XPS measurement was used to investigate the elemental composition and surface chemical environment of the  $\text{Ti}_3\text{C}_2$  MXene sample. Figure 3b depicts the XPS survey spectra of  $\text{Ti}_3\text{C}_2$ , which confirmed the presence of C, Ti, O and F elements. The presence of F and O in  $\text{Ti}_3\text{C}_2$  obtained from the HF etching indicated surface termination ( $\text{Ti}_3\text{C}_2(\text{OH})_2$ ,  $\text{Ti}_3\text{C}_2\text{F}_x$ ), because the enhanced surface activity of  $\text{Ti}_3\text{C}_2$  after the Al layer etching led to reactions with the surrounding  $-\text{O}$  or  $-\text{F}$  [63]. Figure 3c shows the high-resolution Ti 2p XPS spectra, the peaks were corresponding to Ti-C, indicating that the Ti-C binding signal resulted from the Ti atoms in the interior of the MXene layers. As shown in Figure 3d, the C1s spectra mainly exhibited two peaks ascribed to the C-C (284.6 eV) and C-Ti (281.3 eV) bonds [61]. As shown in Figure 3e, the O1s spectra showed three peaks ascribed to Ti-O (529.9 eV), C-O-Ti (530.9 eV) and C-Ti-OH<sub>x</sub> (531.9 eV) [64]. The F 1s spectra in Figure 3f

showed the presence of Ti–F–C bonds located at 684.4 eV and Ti–F–Ti bonds located at 685.6 eV [65]. Overall, the surface of  $\text{Ti}_3\text{C}_2$  contained –O and –F surface functional groups.

### 3.1.2. Structure and Composition of TC-TBCN

Figure 4 shows the morphologies of the TC-TBCN samples. All samples were irregularly shaped powders, and the size of the powders was not uniform, but fine granular materials were coated on the surface. As shown in Figure 4a,b, the size of the 0TC-TBCN sample was smaller than that of TBCN, which indicated the partial decomposition and recrystallization of TBCN during the hydrothermal process. Compared with TBCN, the roughness of the obtained TC-TBCN samples significantly increased after the hydrothermal treatment.  $\text{Ti}_3\text{C}_2$  will be partially decomposed and recrystallized during the hydrothermal process. Thus the accordion-like  $\text{Ti}_3\text{C}_2$  could not be observed in the low-content samples (1TC-TBCN and 2.5TC-TBCN), as shown in Figure 4c,d. In addition, the further increased  $\text{Ti}_3\text{C}_2$  content significantly affected the composites' morphology. The accordion-like structures could be observed in the 5TC-TBCN and 10TC-TBCN samples, as shown in Figure 4e,f.  $\text{C}_3\text{N}_4$  and  $\text{TiO}_2$  were coated on  $\text{Ti}_3\text{C}_2$ . Figure 5 shows the TEM images of the 5TC-TBCN sample. The small crystal particles with clear  $\text{TiO}_2$  lattice fringes were grown on the surface by transforming  $\text{Ti}_3\text{C}_2$  into  $\text{TiO}_2$  through a hydrothermal reaction.

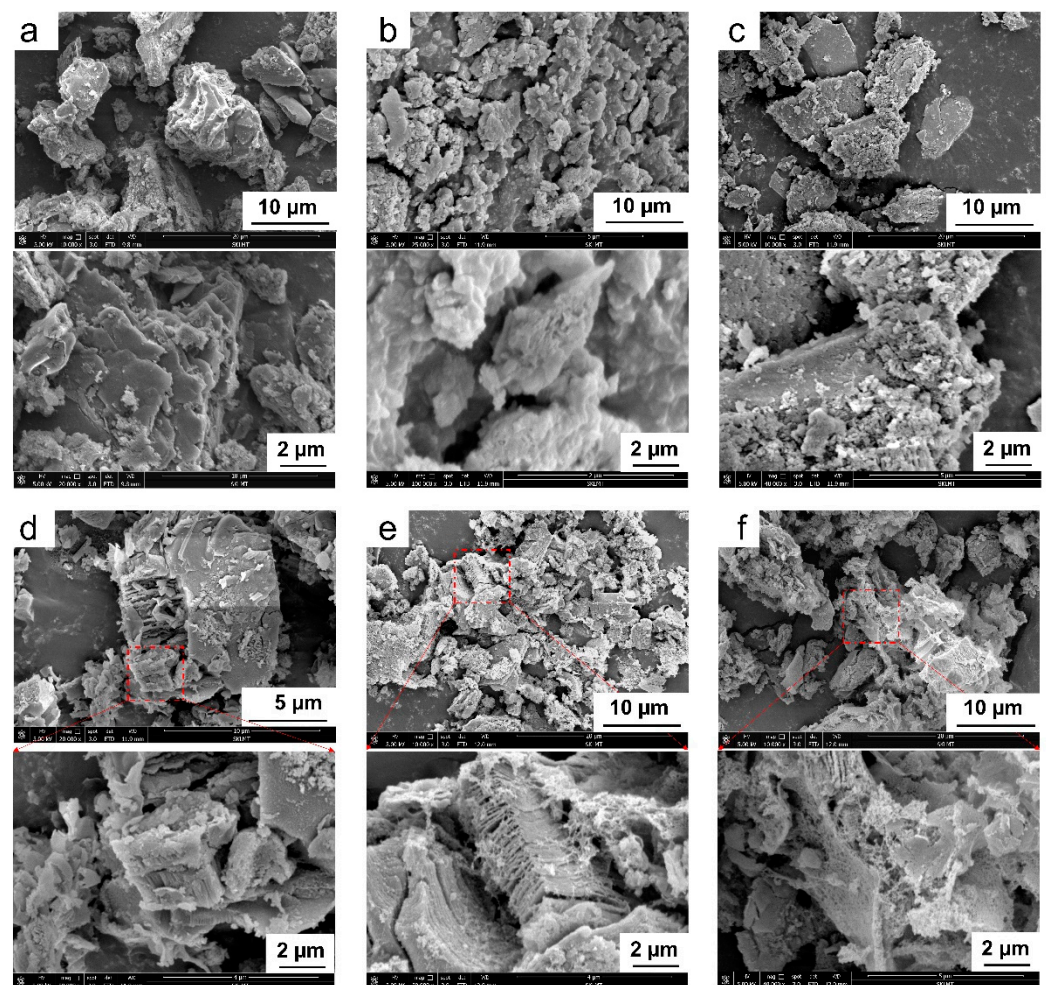


**Figure 4.** SEM images of different samples: (a) TBCN, (b) 0TC-TBCN, (c) 1TC-TBCN, (d) 2.5TC-TBCN, (e) 5TC-TBCN and (f) 10TC-TBCN.

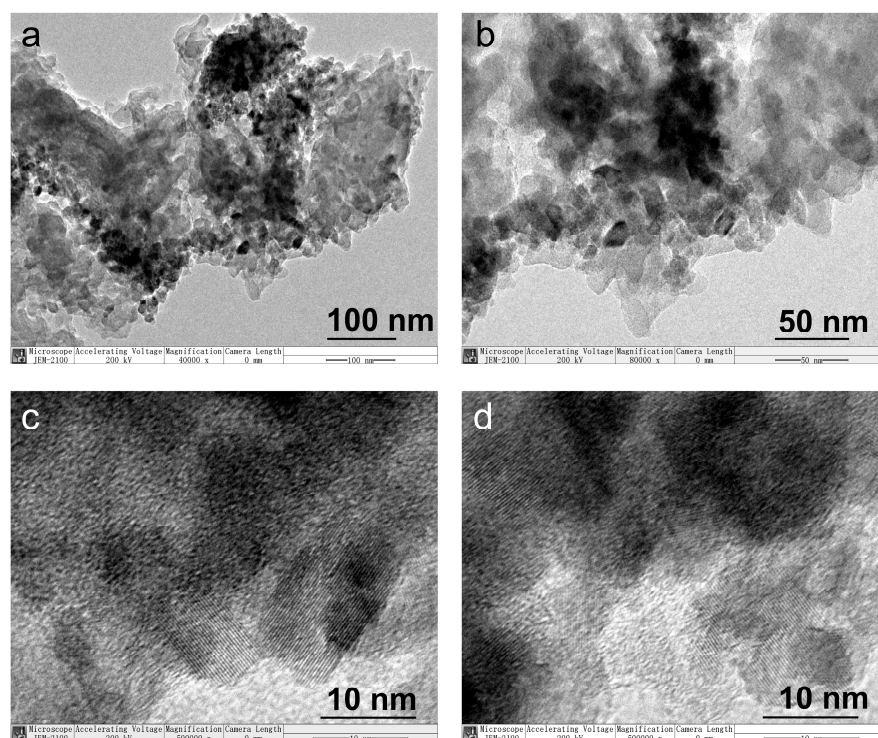


**Figure 5.** TEM images of 5TC-TBCN at different magnifications: (a) 4000 $\times$ ; (b) 8000 $\times$ ; (c–d) 500,000 $\times$ .

An XPS measurement was also used to investigate the surface chemical environment of the 5TC-TBCN sample. Figure 6a depicts the XPS survey spectra of 5TC-TBCN, which confirmed that the elements (C, N, Ti, O and F) existed in the sample. The high-resolution Ti 2p XPS spectra in Figure 6b were shown to possess two peaks of Ti 2p<sub>3/2</sub> and Ti 2p<sub>1/2</sub> that were deconvoluted into two components, Ti–C and Ti–O, indicating the presence of Ti<sub>3</sub>C<sub>2</sub> and TiO<sub>2</sub> in the TC-TBCN sample. The high-resolution C1s spectrum shown in Figure 6c mainly exhibited four peaks. The peak located at 281.3 eV could be ascribed to the C–Ti of Ti<sub>3</sub>C<sub>2</sub>, and the peaks at 284.6 eV, 286.4 eV and 288.6 eV were assigned to the C–C, C–NH<sub>2</sub> and N–C = N bonds in the aromatic skeleton rings of g-C<sub>3</sub>N<sub>4</sub>, respectively. For the N1s spectrum in Figure 6d, the spectrum was fitted into three peaks, the peak at 400.9 eV was ascribed to the C–N–H functional groups, the peaks detected at a binding energy of 399.60 eV was ascribed to tertiary N–(C)<sub>3</sub> and the peak observed at 398.51 eV corresponded to the C–N = C coordination from the sp<sup>2</sup>-bonded N in the triazine rings of g-C<sub>3</sub>N<sub>4</sub> [58]. Moreover, the intensities of these peaks differed from those of g-C<sub>3</sub>N<sub>4</sub> obtained via calcination of melamine, which also indicated that the decomposition and recrystallization of TBCN happened during the hydrothermal process. As shown in Figure 6e, the O1s spectrum showed two peaks at 529.9 eV and 531.9 eV, ascribed to Ti–O and H–O–H from the H<sub>2</sub>O/O<sub>2</sub> adsorption, respectively. The Ti–O bonds confirmed the formation of TiO<sub>2</sub>, which was consistent with the TEM data. No obvious peak in the B 1s XPS spectrum (Figure 6f) indicated that the TiB<sub>2</sub> remaining in the TBCN sample would react with water during the hydrothermal process. The F 1s XPS spectrum is shown in Figure 6f, with peak v at 685.3 eV corresponding to the Ti–F binding energy. The F 1s spectrum in Figure 3f showed the presence of Ti–F bonds at 685.5 eV, confirming the presence of Ti<sub>3</sub>C<sub>2</sub> remaining in the TC-TBCN sample.

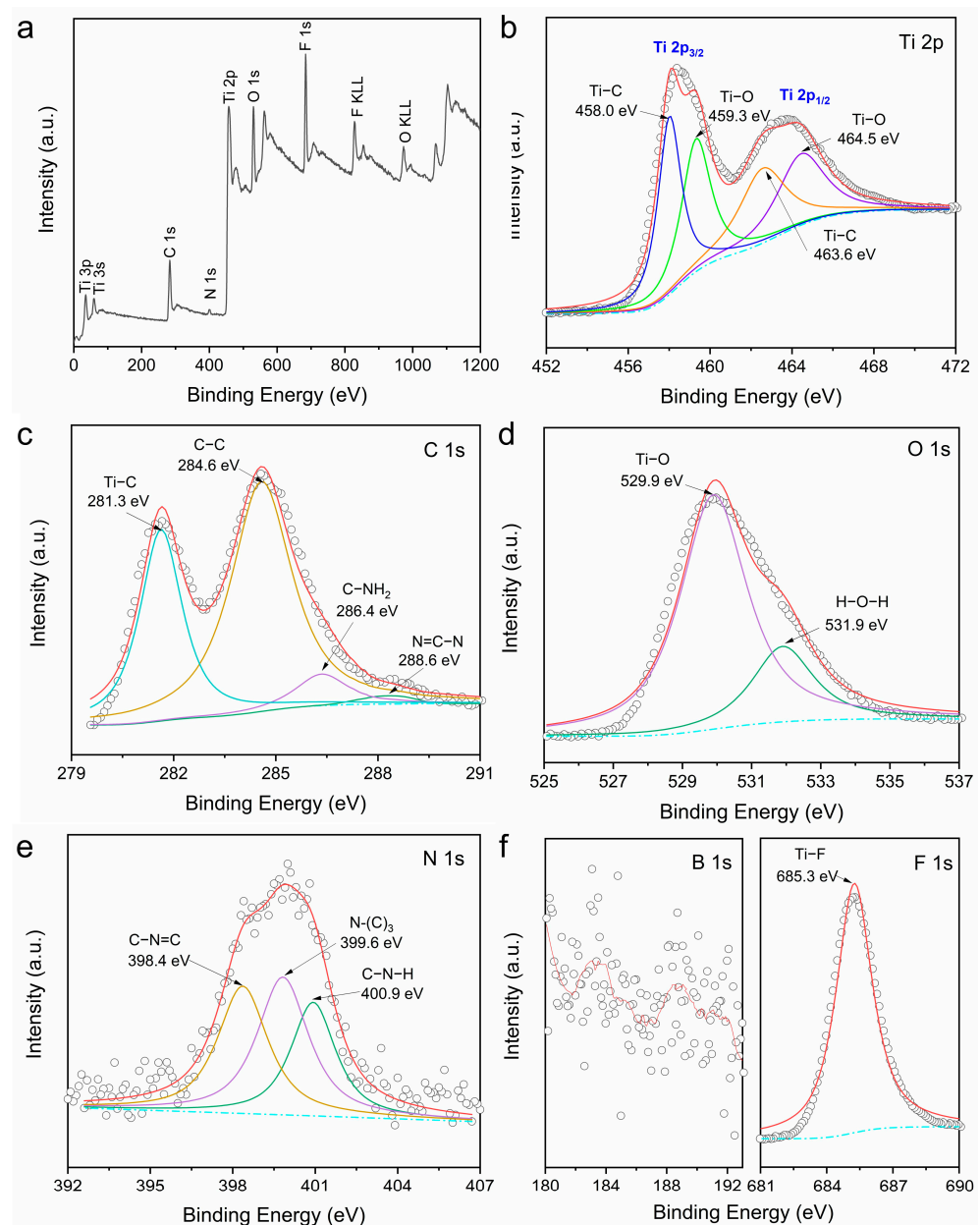


**Figure 6.** XPS spectra of 5TC-TBCN: (a) survey; (b) Ti 2p; (c) C 1s; (d) N 1s; (e) O 1s; (f) B 1s and F 1s.

Figure 7a shows the XRD patterns of the obtained products. The diffraction peaks at  $26.5^\circ$  and  $13.2^\circ$  were consistent with the (002) and (001) planes of  $g\text{-C}_3\text{N}_4$  (PDF#87-1526). Such typical characteristics of interlayer stacking structures indicated the presence of  $g\text{-C}_3\text{N}_4$  in the TBCN and TC-TBCN samples. The characteristic diffraction peaks of  $\text{TiB}_2$  were located at  $34.1^\circ$ ,  $44.4^\circ$ ,  $61.1^\circ$ ,  $68.1^\circ$  and  $68.3^\circ$ , corresponding to the (100), (101), (110), (102) and (111) planes of  $\text{TiB}_2$  (PDF#35-0741), respectively. The peaks located at  $27.4^\circ$ ,  $54.3^\circ$  and  $56.6^\circ$  corresponded to the (110), (211) and (220) planes of rutile (PDF#21-1276), indicating that  $\text{TiB}_2$  could be partially oxidized into rutile  $\text{TiO}_2$  during the thermal treatment at  $550^\circ\text{C}$ . It should be noted here that the most prominent peak located at approximately  $26\text{--}28^\circ$  was the mixed peak from the (002) plane of  $g\text{-C}_3\text{N}_4$ , the (001) plane of  $\text{TiB}_2$  and the (110) plane of rutile  $\text{TiO}_2$ . Incidentally, the peak at approximately  $18.0^\circ$  was related to the carbon phase through the calcination of melamine. All the peaks of  $g\text{-C}_3\text{N}_4$ ,  $\text{TiB}_2$  and rutile  $\text{TiO}_2$  decreased with the  $\text{Ti}_3\text{C}_2$  addition increasing, while the intensities of the peaks located at  $25.3^\circ$ ,  $36.9^\circ$ ,  $48.0^\circ$  and  $53.9^\circ$  corresponded to anatase  $\text{TiO}_2$  (PDF#21-1272) increased with

the  $\text{Ti}_3\text{C}_2$  addition increasing, indicating that the  $\text{Ti}_3\text{C}_2$  or  $\text{TiB}_2$  remaining in TBCN were partially transformed into anatase  $\text{TiO}_2$  during the hydrothermal process.

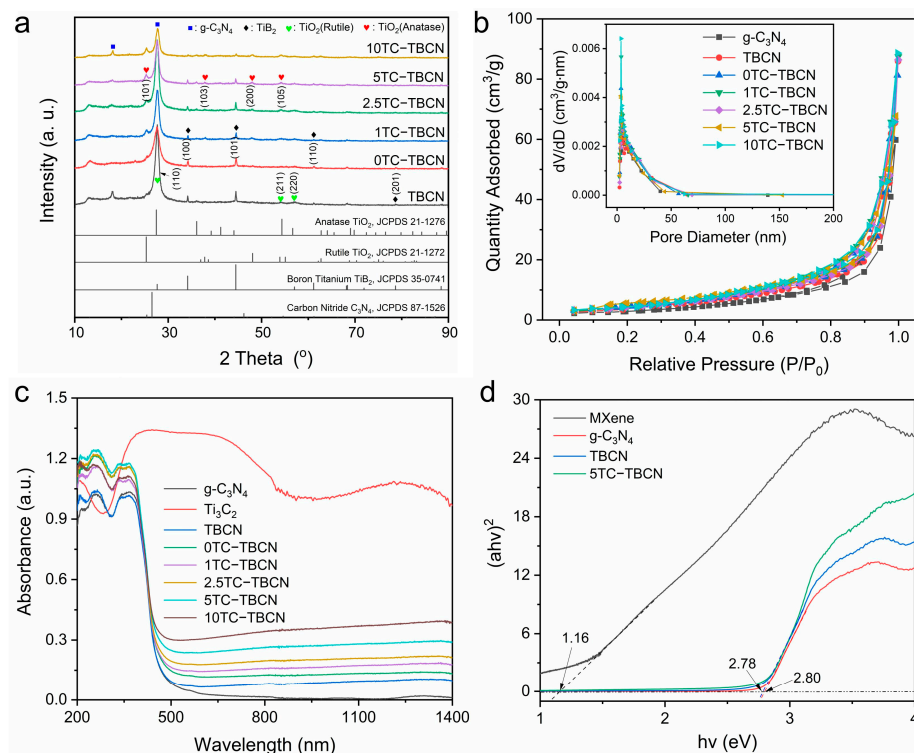


**Figure 7.** (a) XRD patterns, (b)  $\text{N}_2$  adsorption/desorption isotherms and corresponding pore size distribution curves; (c) UV-Vis DRS spectra; (d) the estimated bandgap energies for the different samples.

### 3.1.3. $\text{N}_2$ Sorption Isotherms and Pore Size Distributions

Figure 7b shows the products'  $\text{N}_2$  adsorption-desorption isotherm and pore size distribution plots. The hysteresis loop was of type A, consistent with cylindrical pores. The isotherm's desorption branch could be used to determine the pore size distribution using the Barrett-Joyner-Halenda (BJH) method [58]. The detailed BET surface areas, total pore volumes and average pore diameters of the obtained samples are shown in Table 1. As shown in Table 1, adding  $\text{TiB}_2$  brought along the growing site for  $\text{g-C}_3\text{N}_4$ , enabling the TBCN samples to process larger surface areas than  $\text{g-C}_3\text{N}_4$ . The addition of  $\text{Ti}_3\text{C}_2$  slightly affected the surface areas, and the recrystallization of TBCN led to a shell coated on  $\text{Ti}_3\text{C}_2$ . Thus, the appropriate amount of  $\text{Ti}_3\text{C}_2$  addition brought about proper growing sites, enabling an increased large surface area. 5TC-TBCN had a specific surface area of approximately  $22.034 \text{ m}^2/\text{g}$ , and the smallest average pore size among all the samples.

**Table 1.** BET surface areas, total pore volumes and average pore sizes of the obtained products.

Sample	BET Surface Area ( $\text{m}^2/\text{g}$ )	Total Pore Volume ( $\text{cm}^3/\text{g}$ )	Average Pore Size (nm)
$\text{g-C}_3\text{N}_4$	10.937	0.096	5.223
TBCN	17.384	0.138	3.650
0TC-TBCN	16.829	0.129	3.626
1TC-TBCN	17.231	0.140	3.788
2.5TC-TBCN	16.156	0.137	3.728
5TC-TBCN	22.034	0.106	3.447
10TC-TBCN	15.828	0.142	3.659

### 3.1.4. Optical Absorption Performances of the Samples

The photocatalytic performance of photocatalysts is highly dependent on the light absorption properties of the materials. Figure 7c shows the diffuse reflection absorption spectra of different products. The absorption in 500~1400 nm was enhanced with the increase of  $\text{Ti}_3\text{C}_2$  content, thus, improving the utilization of visible light during the photocatalytic degradation. However, the  $\text{Ti}_3\text{C}_2$  addition did not change the absorption edge of TBCN. Combined with the SEM and XPS results analysis, the added  $\text{Ti}_3\text{C}_2$  only partially converted to  $\text{TiO}_2$ , and some of them remained as the TC-TBCN products, resulting in an enhanced absorption in 500~1400 nm. Meanwhile, more  $\text{Ti}_3\text{C}_2$  would be present in the final product with the increase in  $\text{Ti}_3\text{C}_2$  addition, and, thus, the light absorption abilities in the visible region increased. Moreover,  $\text{Ti}_3\text{C}_2$  increased the light absorption and created a charge transfer channel in the composite photocatalysts. Furthermore, the optical band gap was estimated by applying Tauc's equation. The curves in Figure 7d were obtained using Tauc's formula  $[(\text{Ah}\nu) = \text{B}(\text{h}\nu - \text{Eg})^n]$  ( $n = 2$  for indirect transitions). The values of optical band gaps were 1.16, 2.78, 2.78 and 2.80 eV for  $\text{Ti}_3\text{C}_2$ , TBCN, 5TC-TBCN and  $\text{C}_3\text{N}_4$ , respectively.

### 3.2. Photocatalytic Activity

The photocatalytic performance was evaluated from the degradation of RhB and 4-CP under light irradiation in the solution. The data are presented in Figure 8a, with the photocatalysts with different additions showing some differences after 120 min of light irradiation, and their photocatalytic degradation activities increased first and then decreased with the increased  $\text{Ti}_3\text{C}_2$  content. Figure 8b shows the corresponding kinetic fitting curves, which conformed to the pseudo-first-order kinetics. The degradation rate constants ( $k$ ) of RhB could be calculated from the curves and are shown in Table 2. The 5TC-TBCN displayed the highest  $k$  value of RhB ( $0.01575 \text{ min}^{-1}$ ). Thus, the addition of  $\text{Ti}_3\text{C}_2$  was favorable for the photodegradation of RhB. As expected, the photocatalytic activity of the TC-TBCN sample was higher than that of the absolute  $\text{g-C}_3\text{N}_4$  and TBCN samples due to the introduction of  $\text{Ti}_3\text{C}_2$ , resulting in an enhanced light absorbance and a centered electron acceptor. The cyclic stability of the photocatalysts during practical application was also essential. The cycling degradation of RhB was conducted to measure the recyclability and stability of 5TC-TBCN. As shown in Figure 8c, RhB could maintain a high removal rate, and no significant decrease could be observed after five cycles under the same conditions. Generally, photogenerated holes and electrons can be transferred to the catalyst surface or interface to accede to the oxidation and reduction reactions in the photocatalytic process. Furthermore, to prove the contribution of different reactive groups to the photocatalytic degradation of RhB, isopropyl alcohol (IPA), benzoquinone (BQ), disodium ethylenediaminetetraacetate (EDTA-2Na) and silver nitrate served as trapping agents for the hydroxyl groups (OH), superoxide anion ( $\text{O}_2^-$ ), photogenerated holes ( $\text{h}^+$ ) and electrons ( $\text{e}^-$ ), respectively. As shown in Figure 8d, the removal efficiency of RhB decreased to 14%, 23%, 23%, 34% and 40% in the presence of IPA, EDTA-2Na,  $\text{N}_2$ , BQ and  $\text{AgNO}_3$ , respectively. The degradation rate of RhB was limited in the presence of these scavengers.

Furthermore, the stability of the sample was also confirmed by using FTIR. The samples were obtained from a hydrothermal process, which indicated their excellent stability in water, even hot water. Therefore, FTIR was better for checking the surface change after the photocatalytic reaction. The FTIR spectra are shown in Figure 9. The spectral patterns in  $1100\text{--}1750 \text{ cm}^{-1}$  corresponded to the aromatic C–N stretching vibration and C=N stretching vibrations from  $\text{C}_3\text{N}_4$  [33,66]. Furthermore, the tri-s-triazine unit band was observed at approximately  $810 \text{ cm}^{-1}$ , and the N–H stretching and O–H stretching broad vibration bands from the adsorbed  $\text{H}_2\text{O}$  were observed at  $2800\text{--}3350 \text{ cm}^{-1}$  [67]. There were no significant differences in the curves, indicating no great changes after the photocatalytic reactions.

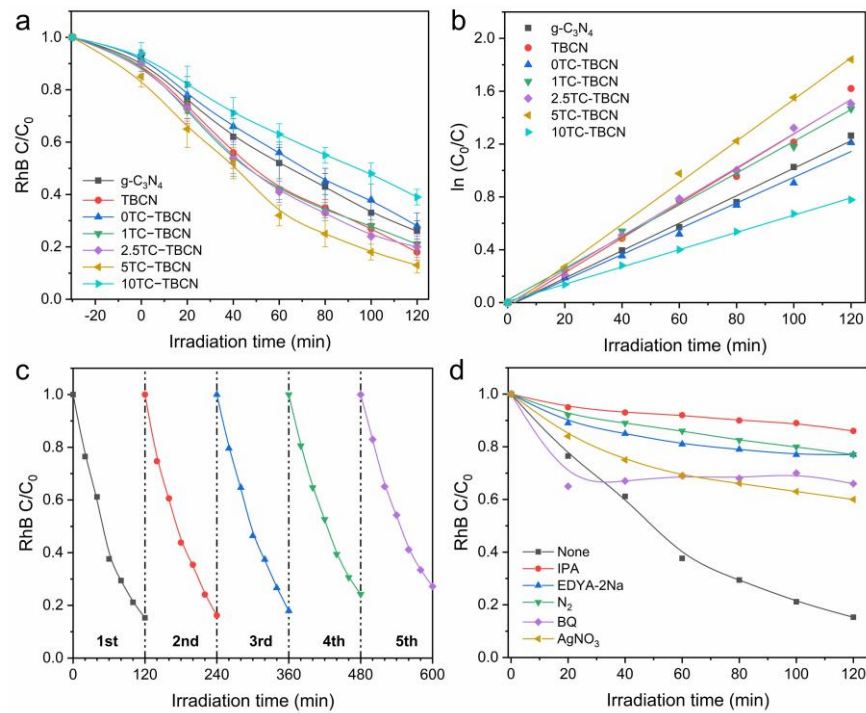


**Figure 8.** (a) Time profiles of the degradation of RhB and (b) the corresponding kinetic fitting curves with irradiation time; (c) photocatalytic stability and (d) photodegradation of RhB over 5TC-TBCN in the presence of different reactive species scavengers. [Catalyst] = 0.5 g/L; [RhB]<sub>0</sub> = 10 ppm.

**Table 2.** Degradation rate constant (k) values of RhB for different photocatalysts.

Sample	k
$g-C_3N_4$	0.0104
TBCN	0.01312
0TC-TBCN	0.00974
1TC-TBCN	0.01202
2.5TC-TBCN	0.01291
5TC-TBCN	0.01575
10TC-TBCN	0.00653

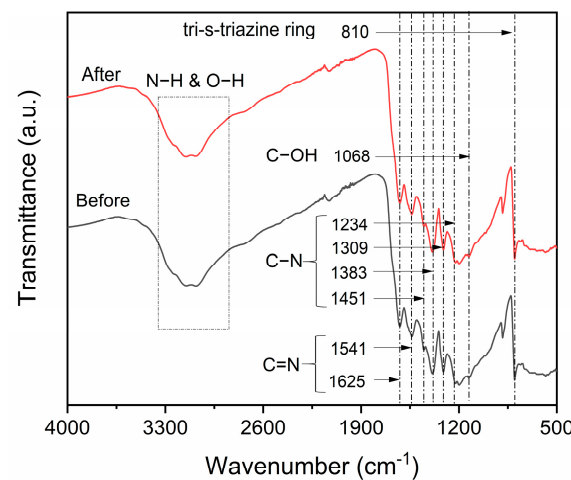


**Figure 9.** FTIR spectra of 5TC-TBCN before and after the reactions.

A similar photocatalytic performance was also conducted in photocatalytic degradation (oxidation) of 4-CP, and the time profiles of the concentrations of 4-CP and  $\text{Cl}^-$  are presented in Figure 10. The measurements began after continuously stirring for 30 min under dark conditions to reach the adsorption equilibrium. HPLC and IC were used to determine the removal of 4-CP, and the data from HPLC and IC were consistent [68]. The TC-TBCN samples showed a similar photocatalytic degradation (oxidation) performance with RhB degradation, and 5TC-TBCN also showed the highest degradation efficiency of 4-CP, indicating that adding  $\text{Ti}_3\text{C}_2$  was also helpful for the photodegradation of 4-CP. As shown in Figure 10, 4-CP and  $\text{Cl}^-$  concentrations were very stable after 120 min of light irradiation alone without the presence of photocatalysts as the blank experiment, showing that 4-CP was hardly self-degradable [10].

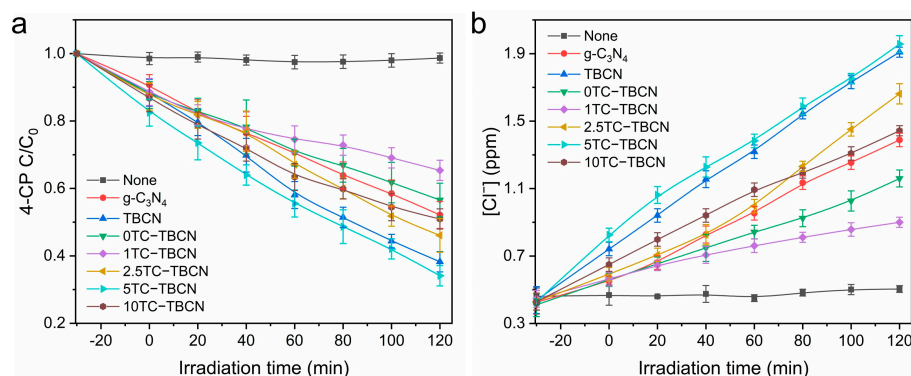


**Figure 10.** (a,b) Time profiles of 4-CP and  $\text{Cl}^-$  concentration during 4-CP removal in the presence of different photocatalysts under light irradiations: [catalyst] = 0.5 g/L;  $[\text{4-CP}]_0 = 10$  ppm.

#### 4. Discussion

The photocatalyst mechanism was investigated by adding different scavengers during the RhB photodegradation process. The TC-TBCN samples obtained from the hydrothermal treatment of  $\text{Ti}_3\text{C}_2$  and TBCN showed excellent photocatalytic degradation activity for RhB and 4-CP. Finally, we proposed the mechanism of TC-TBCN for photocatalysis based on the characterization and photocatalytic performances, as shown in Figure 11 [58,69]. Both g-C<sub>3</sub>N<sub>4</sub> and  $\text{TiO}_2$  could produce electrons and holes under light irradiation, and the addition of  $\text{Ti}_3\text{C}_2$  enhanced the light absorbance capability of the TC-TBCN samples. Figure 10 delineates that the photogenerated electrons on the conduction band (CB) of g-C<sub>3</sub>N<sub>4</sub> would be delivered to the CB of  $\text{TiO}_2$  and further transferred to the  $\text{Ti}_3\text{C}_2$ .  $\text{Ti}_3\text{C}_2$  could act as an intermediate electron acceptor for photogenerated electrons [70,71]. The accumulated electrons on  $\text{Ti}_3\text{C}_2$  could be associated with the adsorbed oxygen reaction to induce the  $\bullet\text{O}_2^-$  active groups for involvement in RhB and 4-CP removal. However, some photogenerated holes on the valence band (VB) of g-C<sub>3</sub>N<sub>4</sub> would combine with the accumulated electrons on  $\text{Ti}_3\text{C}_2$ . Moreover, the electric field of  $\text{Ti}_3\text{C}_2$  and  $\text{TiO}_2$  caused a space charge layer near the  $\text{Ti}_3\text{C}_2/\text{TiO}_2$  interface, resulting in a bending 'upward' VB and CB in the ternary photocatalysts. The Schottky barrier at the interfaces between  $\text{TiO}_2$  and  $\text{Ti}_3\text{C}_2$  inhibited the electron-hole pair recombination, resulting in prolonged electron lifetimes. Thus, the amounts of holes at the VB of  $\text{TiO}_2$  would react with  $\text{H}_2\text{O}$  to form hydroxyl radicals (OH) on the heterogenous photocatalyst's surface, which could efficiently oxidize organic pollutants via the holes at the VB of  $\text{TiO}_2$  into small intermediates, or directly into end products ( $\text{CO}_2$  and  $\text{H}_2\text{O}$ ) [41,61]. The g-C<sub>3</sub>N<sub>4</sub>/ $\text{TiO}_2$  heterojunction and Schottky barrier between  $\text{TiO}_2$  and  $\text{Ti}_3\text{C}_2$  boosted the transfer and separation of the photogenerated carriers, thus, suppressing their recombination [49]. Moreover, the sufficient functional groups on  $\text{Ti}_3\text{C}_2\text{F}_x$  could provide active sites for adsorbing and activating organic pollutants. The enhanced charge separation efficiency could prolong the lifetime of the photogenerated carriers and produce more active species; the abundant

functional groups of the 5TC-TBCN sample provided more active sites, thus, efficiently degrading RhB and 4-CP [54].

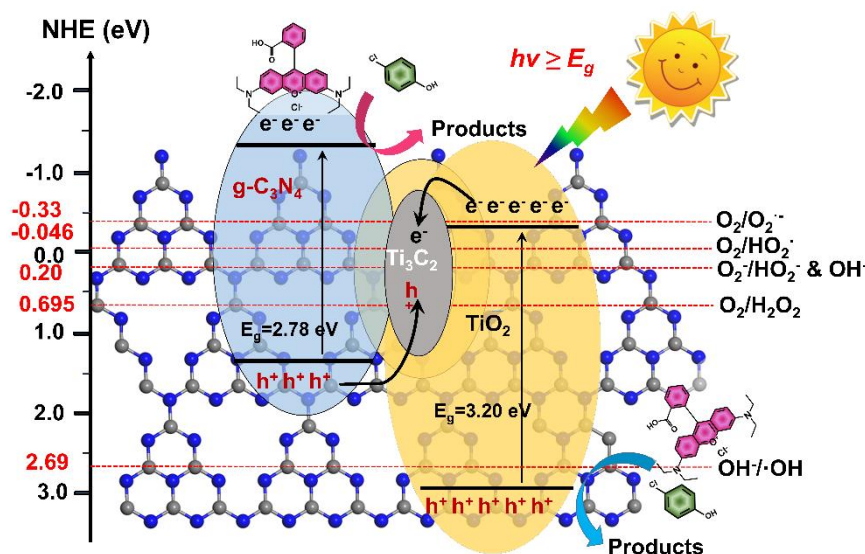


Figure 11. Schematic photocatalytic degradation mechanism over 5TC-TBCN.

## 5. Conclusions

In this research, ternary heterogeneous  $\text{Ti}_3\text{C}_2@\text{TiO}_2/\text{g-C}_3\text{N}_4$  photocatalysts were synthesized through electrostatic self-assembly using a hydrothermal method. The obtained ternary photocatalysts presented a higher photodegradation performance for RhB and 4-CP. The results showed that  $\text{Ti}_3\text{C}_2$  could construct n-type Schottky heterojunctions between  $\text{g-C}_3\text{N}_4$  and  $\text{TiO}_2$ , accepting the photogenerated electrons from the CB of  $\text{g-C}_3\text{N}_4$ ; the multiple built-in electric fields also enhanced the charge transfer and suppressed the recombination of electron-hole pairs, resulting in an enhanced charge separation efficiency. The Schottky barrier between  $\text{TiO}_2$  and  $\text{Ti}_3\text{C}_2$  could also boost the transfer and suppress the recombination. Moreover, the sufficient functional groups in  $\text{Ti}_3\text{C}_2\text{F}_x$  could serve as active sites, which was beneficial for the adsorption and activation of organic pollutants. Thus, the 5TC-TBCN sample process enhanced the photocatalytic degradation of RhB and 4-CP. Ternary heterojunctions such as the one in this study could be efficient photocatalysts in degrading pollutants from organic wastewater.

**Author Contributions:** Conceptualization, J.C. (Jing Chen), J.C. (Jingcai Chang) and Z.H.; supervision, J.C. (Jingcai Chang) and Z.H.; project administration, J.C. (Jing Chen) and Z.H.; writing—original draft preparation, Y.B., J.C. (Jing Chen) and Z.H.; methodology, Y.B. and S.X.; validation, Y.B., J.C. (Jing Chen) and S.X.; investigation, Y.B., S.X. and Z.H.; data curation, Y.B., S.X. and Z.H.; writing—review and editing, X.S., S.Z., J.C. (Jing Chen), X.S., S.Z., J.C. (Jingcai Chang) and Z.H.; funding acquisition, J.C. (Jing Chen) and Z.H. All authors have read and agreed to the published version of the manuscript.

**Funding:** This research was funded by the Natural Science Foundation of China (no. 22278245), the Young Taishan Scholars Program of Shandong Province (no. tsqn.201909026), the Youth Interdisciplinary Science and Innovative Research Groups of Shandong University (no. 2020QNQT014), the Shandong University Future Youth Grant Program (no. 61440089964189) and the Natural Science Basic Research Plan in Shaanxi Province of China (program no. 2019JM-520).

**Institutional Review Board Statement:** Not applicable.

**Informed Consent Statement:** Not applicable.

**Data Availability Statement:** The data presented in this study are available on request from the corresponding author.

**Acknowledgments:** The authors thank Sen Wang from The State Key Laboratory of Microbial Technology, Shandong University, for the assistance in SEM analysis. The authors also thank Fanping Zhu from the Analysis and Test Center of the School of Environmental Science and Engineering, Shandong University, for the assistance in HPLC and UV-Vis analysis.

**Conflicts of Interest:** The authors declare no conflict of interest.

## References

1. Cai, Y.; Sun, T.; Li, G.; An, T. Traditional and emerging water disinfection technologies challenging the control of antibiotic-resistant bacteria and antibiotic resistance genes. *ACS EST Eng.* **2021**, *1*, 1046–1064. [[CrossRef](#)]
2. Xu, J.J.; Gu, H.Y.; Chen, M.D.; Li, X.P.; Zhao, H.W.; Yang, H.B. Dual Z-scheme Bi<sub>3</sub>TaO<sub>7</sub>/Bi<sub>2</sub>S<sub>3</sub>/SnS<sub>2</sub> photocatalyst with high performance for Cr(VI) reduction and TC degradation under visible light irradiation. *Rare Met.* **2022**, *41*, 2417–2428. [[CrossRef](#)]
3. Wang, Z.; Xu, S.; Cai, J.; Ma, J.; Zhao, G. Perspective on photoelectrocatalytic removal of refractory organic pollutants in water systems. *ACS EST Eng.* **2022**, *2*, 1001–1014. [[CrossRef](#)]
4. Cheng, Y.; Cao, T.; Xiao, Z.G.; Zhu, H.J.; Yu, M. Photocatalytic treatment of methyl orange dye wastewater by porous floating ceramsite loaded with cuprous oxide. *Coatings* **2022**, *12*, 286. [[CrossRef](#)]
5. Chen, Z.; Jin, J.; Song, X.; Wei, S.; Zhang, L.; Zhang, S. Effects of low-molecular-weight organics on the photoreduction of bromate in water. *ACS EST Eng.* **2021**, *1*, 581–590. [[CrossRef](#)]
6. Liu, H.; Li, X.X.; Liu, X.Y.; Ma, Z.H.; Yin, Z.Y.; Yang, W.W.; Yu, Y.S. Schiff-base-rich g-C<sub>3</sub>N<sub>4</sub> supported PdAg nanowires as an efficient Mott-Schottky catalyst boosting photocatalytic dehydrogenation of formic acid. *Rare Met.* **2021**, *40*, 808–816. [[CrossRef](#)]
7. Kamoun, O.; Gassoumi, A.; Shkir, M.; Gorji, N.E.; Turki-Kamoun, N. Synthesis and characterization of highly photocatalytic active Ce and Cu co-doped novel spray pyrolysis developed MoO<sub>3</sub> films for photocatalytic degradation of Eosin-Y dye. *Coatings* **2022**, *12*, 823. [[CrossRef](#)]
8. Liu, X.; Huang, W.-Y.; Zhou, Q.; Chen, X.-R.; Yang, K.; Li, D.; Dionysiou, D.D. Ag-decorated 3D flower-like Bi<sub>2</sub>MoO<sub>6</sub>/rGO with boosted photocatalytic performance for removal of organic pollutants. *Rare Met.* **2020**, *40*, 1086–1098. [[CrossRef](#)]
9. He, S.; Chen, Y.; Li, X.; Zeng, L.; Zhu, M. Heterogeneous photocatalytic activation of persulfate for the removal of organic contaminants in water: A critical review. *ACS EST Eng.* **2022**, *2*, 527–546. [[CrossRef](#)]
10. Hunge, Y.M.; Yadav, A.A.; Kang, S.W.; Kim, H. Facile synthesis of multitasking composite of Silver nanoparticle with Zinc oxide for 4-nitrophenol reduction, photocatalytic hydrogen production, and 4-chlorophenol degradation. *J. Alloys Compd.* **2022**, *928*, 167133. [[CrossRef](#)]
11. He, Z.; Zhang, J.; Li, X.; Guan, S.; Dai, M.; Wang, S. 1D/2D heterostructured photocatalysts: From design and unique properties to their environmental applications. *Small* **2020**, *16*, 2005051. [[CrossRef](#)]
12. Zhang, S.; He, Z.; Li, X.; Zhang, J.; Zang, Q.; Wang, S. Building heterogeneous nanostructures for photocatalytic ammonia decomposition. *Nanoscale Adv.* **2020**, *2*, 3610–3623. [[CrossRef](#)] [[PubMed](#)]
13. Dai, M.; He, Z.; Zhang, P.; Li, X.; Wang, S. ZnWO<sub>4</sub>-ZnIn<sub>2</sub>S<sub>4</sub> S-scheme heterojunction for enhanced photocatalytic H<sub>2</sub> evolution. *J. Mater. Sci. Technol.* **2022**, *122*, 231–242. [[CrossRef](#)]
14. Zhang, G.; Ruan, J.; Du, T. Recent advances on photocatalytic and electrochemical oxidation for ammonia treatment from water/wastewater. *ACS EST Eng.* **2021**, *1*, 310–325. [[CrossRef](#)]
15. Tonda, S.; Kumar, S.; Bhardwaj, M.; Yadav, P.; Ogale, S. g-C<sub>3</sub>N<sub>4</sub>/NiAl-LDH 2D/2D hybrid heterojunction for high-performance photocatalytic reduction of CO<sub>2</sub> into renewable fuels. *ACS Appl. Mater. Interfaces* **2018**, *10*, 2667–2678. [[CrossRef](#)] [[PubMed](#)]
16. Zhang, S.; Dai, M.; Guo, J.; Wang, G.; Wang, S.; He, Z. Stable Ti<sup>3+</sup> in B-TiO<sub>2</sub>/BN based hybrids for efficient photocatalytic reduction. *Chem. Eng. J. Adv.* **2022**, *11*, 100333. [[CrossRef](#)]
17. Liu, D.; Zhang, S.; Wang, J.; Peng, T.; Li, R. Direct Z-Scheme 2D/2D photocatalyst based on ultrathin g-C<sub>3</sub>N<sub>4</sub> and WO<sub>3</sub> nanosheets for efficient visible-light-driven H<sub>2</sub> generation. *ACS Appl. Mater. Interfaces* **2019**, *11*, 27913–27923. [[CrossRef](#)]
18. Dai, M.; He, Z.; Cao, W.; Zhang, J.; Chen, W.; Jin, Q.; Que, W.; Wang, S. Rational construction of S-scheme BN/MXene/ZnIn<sub>2</sub>S<sub>4</sub> heterojunction with interface engineering for efficient photocatalytic hydrogen production and chlorophenols degradation. *Sep. Purif. Technol.* **2023**, *309*, 123004. [[CrossRef](#)]
19. Saleem, Z.; Pervaiz, E.; Yousaf, M.U.; Niazi, M.B.K. Two-dimensional materials and composites as potential water splitting photocatalysts: A review. *Catalysts* **2020**, *10*, 464. [[CrossRef](#)]
20. Ngullie, R.C.; Alaswad, S.O.; Bhuvanewari, K.; Shanmugam, P.; Pazhanivel, T.; Arunachalam, P. Synthesis and characterization of efficient ZnO/g-C<sub>3</sub>N<sub>4</sub> nanocomposites photocatalyst for photocatalytic degradation of methylene blue. *Coatings* **2020**, *10*, 500. [[CrossRef](#)]
21. Yu, H.; Dai, M.; Zhang, J.; Chen, W.; Jin, Q.; Wang, S.; He, Z. Interface engineering in 2D/2D heterogeneous photocatalysts. *Small* **2022**, *19*, 2205767. [[CrossRef](#)] [[PubMed](#)]
22. Ren, D.; Liang, Z.; Ng, Y.H.; Zhang, P.; Xiang, Q.; Li, X. Strongly coupled 2D-2D nanojunctions between P-doped Ni<sub>2</sub>S (Ni<sub>2</sub>SP) cocatalysts and CdS nanosheets for efficient photocatalytic H<sub>2</sub> evolution. *Chem. Eng. J.* **2020**, *390*, 124496. [[CrossRef](#)]
23. Shen, R.C.; Zhang, L.P.; Chen, X.Z.; Jaroniec, M.; Li, N.; Li, X. Integrating 2D/2D CdS/alpha-Fe<sub>2</sub>O<sub>3</sub> ultrathin bilayer Z-scheme heterojunction with metallic beta-NiS nanosheet-based ohmic junction for efficient photocatalytic H<sub>2</sub> evolution. *Appl. Catal. B-Environ.* **2020**, *266*, 118619. [[CrossRef](#)]

24. He, Z.; Kim, C.; Lin, L.H.; Jeon, T.H.; Lin, S.; Wang, X.C.; Choi, W. Formation of heterostructures via direct growth CN on h-BN porous nanosheets for metal-free photocatalysis. *Nano Energy* **2017**, *42*, 58–68. [[CrossRef](#)]
25. Zhou, A.Q.; Yang, J.M.; Zhu, X.W.; Zhu, X.L.; Liu, J.Y.; Zhong, K.; Chen, H.X.; Chu, J.Y.; Du, Y.S.; Song, Y.H.; et al. Self-assembly construction of NiCo LDH/ultrathin g-C<sub>3</sub>N<sub>4</sub> nanosheets photocatalyst for enhanced CO<sub>2</sub> reduction and charge separation mechanism study. *Rare Met.* **2022**, *41*, 2118–2128. [[CrossRef](#)]
26. Zhang, S.J.; He, Z.L.; Xu, S.S.; Li, X.; Zhang, J.; Zhan, X.P.; Dai, M.; Wang, S.G. In situ liquid-phase growth strategies of g-C<sub>3</sub>N<sub>4</sub> solar-driven heterogeneous catalysts for environmental applications. *Solar RRL* **2021**, *5*, 2100233. [[CrossRef](#)]
27. Liao, Y.-W.; Yang, J.; Wang, G.-H.; Wang, J.; Wang, K.; Yan, S.D. Hierarchical porous NiO as a noble-metal-free cocatalyst for enhanced photocatalytic H<sub>2</sub> production of nitrogen-deficient g-C<sub>3</sub>N<sub>4</sub>. *Rare Met.* **2021**, *41*, 396–405. [[CrossRef](#)]
28. Shen, R.C.; Liu, W.; Ren, D.D.; Xie, J.; Li, X. Co<sub>1.4</sub>Ni<sub>0.6</sub>P cocatalysts modified metallic carbon black/g-C<sub>3</sub>N<sub>4</sub> nanosheet Schottky heterojunctions for active and durable photocatalytic H<sub>2</sub> production. *Appl. Surf. Sci.* **2019**, *466*, 393–400. [[CrossRef](#)]
29. Zhang, X.; Li, M.J.; Liu, C.; Zhang, Z.Y.; Zhang, F.C.; Liu, Q.P. Enhanced the efficiency of photocatalytic degradation of methylene blue by construction of Z-scheme g-C<sub>3</sub>N<sub>4</sub>/BiVO<sub>4</sub> heterojunction. *Coatings* **2021**, *11*, 1027. [[CrossRef](#)]
30. Akhundi, A.; Moshfegh, A.Z.; Habibi-Yangjeh, A.; Sillanpaa, M. Simultaneous dual-functional photocatalysis by g-C<sub>3</sub>N<sub>4</sub>-based nanostructures. *ACS EST Eng.* **2022**, *2*, 564–585. [[CrossRef](#)]
31. Fernandez-Catala, J.; Greco, R.; Navlani-Garcia, M.; Cao, W.; Berenguer-Murcia, A.; Cazorla-Amoros, D. g-C<sub>3</sub>N<sub>4</sub>-based direct Z-scheme photocatalysts for environmental applications. *Catalysts* **2022**, *12*, 1137. [[CrossRef](#)]
32. Cheng, L.; Zhang, H.; Li, X.; Fan, J.; Xiang, Q. Carbon-graphitic carbon nitride hybrids for heterogeneous photocatalysis. *Small* **2021**, *17*, 2005231. [[CrossRef](#)]
33. Zhang, Y.; Zhao, S.M.; Su, Q.W.; Xu, J.L. Visible light response ZnO-C<sub>3</sub>N<sub>4</sub> thin film photocatalyst. *Rare Met.* **2021**, *40*, 96–104. [[CrossRef](#)]
34. Dao, D.Q.; Nguyen, T.K.A.; Pham, T.T.; Shin, E.W. Synergistic effect on photocatalytic activity of Co-doped NiTiO<sub>3</sub>/g-C<sub>3</sub>N<sub>4</sub> composites under visible light irradiation. *Catalysts* **2020**, *10*, 1332. [[CrossRef](#)]
35. Yan, R.; Zada, A.; Sun, L.; Li, Z.J.; Mu, Z.Y.; Chen, S.Y.; Yang, F.; Sun, J.H.; Bai, L.L.; Qu, Y.; et al. Comparative study of metal oxides and phosphate modification with different mechanisms over g-C<sub>3</sub>N<sub>4</sub> for visible-light photocatalytic degradation of metribuzin. *Rare Met.* **2021**, *41*, 155–165. [[CrossRef](#)]
36. Koci, K.; Reli, M.; Troppova, I.; Sihor, M.; Bajcarova, T.; Ritz, M.; Pavlovsky, J.; Praus, P. Photocatalytic decomposition of N<sub>2</sub>O by using nanostructured graphitic carbon nitride/zinc oxide photocatalysts immobilized on foam. *Catalysts* **2019**, *9*, 735. [[CrossRef](#)]
37. Zhang, H.; Li, L.; Li, Q.Q.; Ma, T.; Gao, J.Q.; Xue, J.B.; Gao, S. Graphitic carbon nitride loaded with bismuth nanoparticles displays antibacterial photocatalytic activity. *Rare Met.* **2022**, *41*, 1570–1582. [[CrossRef](#)]
38. Li, Y.; Zhang, M.Q.; Liu, Y.F.; Zhao, Q.H.; Li, X.; Zhou, Q.Y.; Chen, Y.F.; Wang, S.F. Construction of bronze TiO<sub>2</sub>/Ti<sub>3</sub>C<sub>2</sub> MXene/Ag<sub>3</sub>PO<sub>4</sub> ternary composite photocatalyst toward high photocatalytic performance. *Catalysts* **2022**, *12*, 599. [[CrossRef](#)]
39. Xiao, L.H.; Li, X.; Zhang, J.; He, Z.L. MgB<sub>4</sub> MXene-like nanosheets for photocatalytic hydrogen evolution. *ACS Appl. Nano Mater.* **2021**, *4*, 12779–12787. [[CrossRef](#)]
40. Zhang, S.; Zhang, M.; Xiong, W.; Long, J.; Xu, Y.; Yang, L.; Dai, W. Constructing active sites on self-supporting Ti<sub>3</sub>C<sub>2</sub>T<sub>x</sub> (T = OH) nanosheets for enhanced photocatalytic CO<sub>2</sub> reduction into alcohols. *Catalysts* **2022**, *12*, 1594. [[CrossRef](#)]
41. You, Z.; Liao, Y.; Li, X.; Fan, J.; Xiang, Q. State-of-the-art recent progress in MXene-based photocatalysts: A comprehensive review. *Nanoscale* **2021**, *13*, 9463–9504. [[CrossRef](#)]
42. Li, Y.; Yang, Y.L.; Chen, G.; Fan, J.J.; Xiang, Q.J. Au cluster anchored on TiO<sub>2</sub>/Ti<sub>3</sub>C<sub>2</sub> hybrid composites for efficient photocatalytic CO<sub>2</sub> reduction. *Rare Met.* **2022**, *41*, 3045–3059. [[CrossRef](#)]
43. Govindan, B.; Madhu, R.; Abu Haija, M.; Kusmartsev, F.V.; Banat, F. Pd-decorated 2D MXene (2D Ti<sub>3</sub>C<sub>2</sub>T<sub>x</sub>) as a high-performance electrocatalyst for reduction of carbon dioxide into fuels toward climate change mitigation. *Catalysts* **2022**, *12*, 1180. [[CrossRef](#)]
44. Wang, Z.; Yu, K.; Gong, S.; Mao, H.; Huang, R.; Zhu, Z. Cu<sub>3</sub>BiS<sub>3</sub>/MXenes with Excellent Solar-Thermal Conversion for Continuous and Efficient Seawater Desalination. *ACS Appl. Mater. Interfaces* **2021**, *13*, 16246–16258. [[CrossRef](#)]
45. Yang, Y.; Zhang, D.; Fan, J.; Liao, Y.; Xiang, Q. Construction of an ultrathin S-Scheme heterojunction based on few-layer g-C<sub>3</sub>N<sub>4</sub> and monolayer Ti<sub>3</sub>C<sub>2</sub>T<sub>x</sub> MXene for photocatalytic CO<sub>2</sub> reduction. *Solar RRL* **2020**, *5*, 2000351. [[CrossRef](#)]
46. Li, Y.; Zhang, D.; Feng, X.; Liao, Y.; Wen, Q.; Xiang, Q. Truncated octahedral bipyramidal TiO<sub>2</sub>/MXene Ti<sub>3</sub>C<sub>2</sub> hybrids with enhanced photocatalytic H<sub>2</sub> production activity. *Nanoscale Adv.* **2019**, *1*, 1812–1818. [[CrossRef](#)] [[PubMed](#)]
47. Ta, Q.T.H.; Tran, N.M.; Noh, J.S. Rice crust-like ZnO/Ti<sub>3</sub>C<sub>2</sub>T<sub>x</sub> MXene hybrid structures for improved photocatalytic activity. *Catalysts* **2020**, *10*, 1140. [[CrossRef](#)]
48. Huang, G.M.; Li, S.Z.; Liu, L.J.; Zhu, L.F.; Wang, Q. Ti<sub>3</sub>C<sub>2</sub> MXene-modified Bi<sub>2</sub>WO<sub>6</sub> nanoplates for efficient photodegradation of volatile organic compounds. *Appl. Surf. Sci.* **2020**, *503*, 144183. [[CrossRef](#)]
49. Cai, T.; Wang, L.L.; Liu, Y.T.; Zhang, S.Q.; Dong, W.Y.; Chen, H.; Yi, X.Y.; Yuan, J.L.; Xia, X.N.; Liu, C.B.; et al. Ag<sub>3</sub>PO<sub>4</sub>/Ti<sub>3</sub>C<sub>2</sub> MXene interface materials as a Schottky catalyst with enhanced photocatalytic activities and anti-photocorrosion performance. *Appl. Catal. B-Environ.* **2018**, *239*, 545–554. [[CrossRef](#)]
50. Zhao, C.; Yang, X.; Han, C.; Xu, J. Sacrificial agent-free photocatalytic oxygen evolution from water splitting over Ag<sub>3</sub>PO<sub>4</sub>/MXene hybrids. *Solar RRL* **2019**, *4*, 1900434. [[CrossRef](#)]
51. Wang, J.H.; Shen, Y.F.; Liu, S.Q.; Zhang, Y.J. Single 2D MXene precursor-derived TiO<sub>2</sub> nanosheets with a uniform decoration of amorphous carbon for enhancing photocatalytic water splitting. *Appl. Catal. B-Environ.* **2020**, *270*, 118885. [[CrossRef](#)]

52. Low, J.X.; Zhang, L.Y.; Tong, T.; Shen, B.J.; Yu, J.G. TiO<sub>2</sub>/MXene Ti<sub>3</sub>C<sub>2</sub> composite with excellent photocatalytic CO<sub>2</sub> reduction activity. *J. Catal.* **2018**, *361*, 255–266. [[CrossRef](#)]
53. He, F.; Zhu, B.C.; Cheng, B.; Yu, J.G.; Ho, W.K.; Macyk, W. 2D/2D/0D TiO<sub>2</sub>/C<sub>3</sub>N<sub>4</sub>/Ti<sub>3</sub>C<sub>2</sub> MXene composite S-scheme photocatalyst with enhanced CO<sub>2</sub> reduction activity. *Appl. Catal. B-Environ.* **2020**, *272*, 119006. [[CrossRef](#)]
54. Zhang, X.M.; Nie, J.L.; Rao, F.; Liu, H.X.; Wang, Y.J.; Qu, D.Y.; Wu, W.W.; Zhong, P.; Zhu, G.Q. Ti<sub>3</sub>C<sub>2</sub>@TiO<sub>2</sub>/g-C<sub>3</sub>N<sub>4</sub> heterojunction photocatalyst with improved charge transfer for enhancing visible-light NO selective removal. *Ceram. Int.* **2021**, *47*, 31302–31310. [[CrossRef](#)]
55. Chang, B.; Guo, Y.; Wu, D.; Li, L.; Yang, B.; Wang, J. Plasmon-enabled N<sub>2</sub> photofixation on partially reduced Ti<sub>3</sub>C<sub>2</sub> MXene. *Chem. Sci.* **2021**, *12*, 11213–11224. [[CrossRef](#)]
56. Sun, C.; Chen, Z.; Cui, J.; Li, K.; Qu, H.; Xie, H.; Zhong, Q. Site-exposed Ti<sub>3</sub>C<sub>2</sub> MXene anchored in N-defect g-C<sub>3</sub>N<sub>4</sub> heterostructure nanosheets for efficient photocatalytic N<sub>2</sub> fixation. *Catal. Sci. Technol.* **2021**, *11*, 1027–1038. [[CrossRef](#)]
57. Wei, H.; Jiang, Q.; Ampelli, C.; Chen, S.; Perathoner, S.; Liu, Y.; Centi, G. Enhancing N<sub>2</sub> fixation activity by converting Ti<sub>3</sub>C<sub>2</sub> MXenes nanosheets to nanoribbons. *ChemSusChem* **2020**, *13*, 5614–5619. [[CrossRef](#)]
58. Yu, H.; Xu, S.; Zhang, S.; Wang, S.; He, Z. In-situ construction of core-shell structured TiB<sub>2</sub>-TiO<sub>2</sub>@g-C<sub>3</sub>N<sub>4</sub> for efficient photocatalytic degradation. *Appl. Surf. Sci.* **2022**, *579*, 152201. [[CrossRef](#)]
59. Liu, Q.; Tan, X.; Wang, S.; Ma, F.; Znad, H.; Shen, Z.; Liu, L.; Liu, S. MXene as a non-metal charge mediator in 2D layered CdS@Ti<sub>3</sub>C<sub>2</sub>@TiO<sub>2</sub> composites with superior Z-scheme visible light-driven photocatalytic activity. *Environ. Sci. Nano* **2019**, *6*, 3158–3169. [[CrossRef](#)]
60. Yang, C.; Tan, Q.Y.; Li, Q.; Zhou, J.; Fan, J.J.; Li, B.; Sun, J.; Lv, K.L. 2D/2D Ti<sub>3</sub>C<sub>2</sub> MXene/g-C<sub>3</sub>N<sub>4</sub> nanosheets heterojunction for high efficient CO<sub>2</sub> reduction photocatalyst: Dual effects of urea. *Appl. Catal. B-Environ.* **2020**, *268*, 118738. [[CrossRef](#)]
61. Chen, L.; Ye, X.Y.; Chen, S.; Ma, L.; Wang, Z.P.; Wang, Q.T.; Hua, N.B.; Xiao, X.Q.; Cai, S.G.; Liu, X.H. Ti<sub>3</sub>C<sub>2</sub> MXene nanosheet/TiO<sub>2</sub> composites for efficient visible light photocatalytic activity. *Ceram. Int.* **2020**, *46*, 25895–25904. [[CrossRef](#)]
62. Zhao, G.; Lv, H.; Zhou, Y.; Zheng, X.; Wu, C.; Xu, C. Self-assembled sandwich-like mXene-derived nanocomposites for enhanced electromagnetic wave absorption. *ACS Appl. Mater. Interfaces* **2018**, *10*, 42925–42932. [[CrossRef](#)] [[PubMed](#)]
63. Hu, T.; Wang, J.; Zhang, H.; Li, Z.; Hu, M.; Wang, X. Vibrational properties of Ti<sub>3</sub>C<sub>2</sub> and Ti<sub>3</sub>C<sub>2</sub>T<sub>2</sub> (T = O, F, OH) monosheets by first-principles calculations: A comparative study. *Phys. Chem. Chem. Phys.* **2015**, *17*, 9997–10003. [[CrossRef](#)] [[PubMed](#)]
64. Liu, A.; Gao, M.; Ren, X.; Meng, F.; Yang, Y.; Yang, Q.; Guan, W.; Gao, L.; Liang, X.; Ma, T. A two-dimensional Ru@MXene catalyst for highly selective ambient electrocatalytic nitrogen reduction. *Nanoscale* **2020**, *12*, 10933–10938. [[CrossRef](#)] [[PubMed](#)]
65. Tanvir, A.; Sobolčiak, P.; Popelka, A.; Mrlik, M.; Spitalsky, Z.; Micusik, M.; Prokes, J.; Krupa, I. Electrically conductive, transparent polymeric nanocomposites modified by 2D Ti<sub>3</sub>C<sub>2</sub>T<sub>x</sub> (MXene). *Polymers* **2019**, *11*, 1272. [[CrossRef](#)] [[PubMed](#)]
66. Feng, Y.B.; Du, Y.; Du, M.X.; Li, Z.F.; He, Z.L.; Yang, K.; Lv, X.J.; Jiang, N.; Liu, Y. Facile constructing novel 3D porous g-C<sub>3</sub>N<sub>4</sub>/BiOBr<sub>0.2</sub>IO<sub>0.8</sub> hybrids: Efficient charge separation for visible-light photocatalysis. *J. Alloys Compd.* **2018**, *767*, 241–252. [[CrossRef](#)]
67. He, Z.; Que, W.; Chen, J.; He, Y.; Wang, G. Surface chemical analysis on the carbon-doped mesoporous TiO<sub>2</sub> photocatalysts after post-thermal treatment: XPS and FTIR characterization. *J. Phys. Chem. Solids* **2013**, *74*, 924–928. [[CrossRef](#)]
68. Cho, Y.-J.; Kim, H.-i.; Lee, S.; Choi, W. Dual-functional photocatalysis using a ternary hybrid of TiO<sub>2</sub> modified with graphene oxide along with Pt and fluoride for H<sub>2</sub>-producing water treatment. *J. Catal.* **2015**, *330*, 387–395. [[CrossRef](#)]
69. Cui, S.-S.; Liu, X.; Shi, Y.-B.; Ding, M.-Y.; Yang, X.-F. Construction of atomic-level charge transfer channel in Bi<sub>12</sub>O<sub>17</sub>Cl<sub>2</sub>/MXene heterojunctions for improved visible-light photocatalytic performance. *Rare Met.* **2022**, *41*, 2405–2416. [[CrossRef](#)]
70. Jiang, Z.; Chen, Q.; Zheng, Q.; Shen, R.; Zhang, P.; Li, X. Constructing 1D/2D schottky-based heterojunctions between Mn<sub>0.2</sub>Cd<sub>0.8</sub>S nanorods and Ti<sub>3</sub>C<sub>2</sub> nanosheets for boosted photocatalytic H<sub>2</sub> evolution. *Acta Phys.-Chim. Sin.* **2021**, *37*, 2010059.
71. Bai, J.; Shen, R.; Chen, W.; Xie, J.; Zhang, P.; Jiang, Z.; Li, X. Enhanced photocatalytic H<sub>2</sub> evolution based on a Ti<sub>3</sub>C<sub>2</sub>/Zn<sub>0.7</sub>Cd<sub>0.3</sub>S/Fe<sub>2</sub>O<sub>3</sub> Ohmic/S-scheme hybrid heterojunction with cascade 2D coupling interfaces. *Chem. Eng. J.* **2022**, *429*, 132587. [[CrossRef](#)]

**Disclaimer/Publisher's Note:** The statements, opinions and data contained in all publications are solely those of the individual author(s) and contributor(s) and not of MDPI and/or the editor(s). MDPI and/or the editor(s) disclaim responsibility for any injury to people or property resulting from any ideas, methods, instructions or products referred to in the content.